A&A 547, A55 (2012)
DOI: 10.1051/0004-6361/201219765

Astronomy & Astrophysics

A brown dwarf orbiting an M-dwarf: MOA 2009–BLG–411L⋆

E. Bachelet[1,44], P. Fouqué[1,44], C. Han[2,24], A. Gould[2,7], M. D. Albrow[1,8], J.-P. Beaulieu[1,11], E. Bertin[11], I. A. Bond[4,30], G. W. Christie[2,64], D. Heyrovský[48], K. Horne[1,5,13], U. G. Jørgensen[6,45], D. Maoz[2,63], M. Mathiasen[6,45], N. Matsunaga[66], J. McCormick[2,65], J. Menzies[1,22], D. Nataf[7], T. Natusch[2,64,79], N. Oi[68], N. Renon[69], Y. Tsapras[5,39,60], A. Udalski[3,27], J. C. Yee[2,7], V. Batista[11], D. P. Bennett[4,15], S. Brillant[9], J. A. R. Caldwell[15], A. Cassan[1,11], A. Cole[19], K. H. Cook[16], C. Coutures[11], S. Dieters[11], M. Dominik[6,13,⋆⋆], D. Dominis Prester[17], J. Donatowicz[18], J. Greenhill[19], N. Kains[5,10,13], S. R. Kane[20], J.-B. Marquette[11], R. Martin[21], K. R. Pollard[8], K. C. Sahu[23], R. A. Street[5,39,43], J. Wambsganss[6,12], A. Williams[21], M. Zub[6,12]
(The PLANET Collaboration)[1],
M. Bos[75], Subo Dong[78], J. Drummond[62], B. S. Gaudi[7], D. Graff, J. Janczak[7], S. Kaspi[63], S. Kozłowski[3,7,27], C.-U. Lee[71], L. A. G. Monard[26], J. A. Muñoz[76], B.-G. Park[71], R. W. Pogge[7], D. Polishook[63], A. Shporer[63]
(The μFUN Collaboration)[2],
F. Abe[31], C. S.Botzler[35], A. Fukui[80], K. Furusawa[31], J. B. Hearnshaw[8], Y. Itow[31], A. V. Korpela[38], C. H. Ling[30], K. Masuda[31], Y. Matsubara[31], N. Miyake[31], Y. Muraki[33], K. Ohnishi[34], N. J. Rattenbury[5,35], To. Saito[36], D. Sullivan[38], T. Sumi[31], D. Suzuki[31], W. L. Sweatman[4,30], P. J. Tristram[29], K. Wada[31]
(The MOA Collaboration)[4],
A. Allan[41], M. F. Bode[40], D. M. Bramich[10], N. Clay[40], S. N. Fraser[40], E. Hawkins[39], E. Kerins[32], T. A. Lister[39], C. J. Mottram[40], E. S. Saunders[39,41], C. Snodgrass[6,9], I. A. Steele[40], P. J. Wheatley[42]
(The RoboNet-II Collaboration)[5],
V. Bozza[50], P. Browne[13], M. J. Burgdorf[5,57,58], S. Calchi Novati[50], S. Dreizler[53], F. Finet[54], M. Glitrup[74], F. Grundahl[74], K. Harpsøe[45], F. V. Hessman[53], T. C. Hinse[45,51,71], M. Hundertmark[53], C. Liebig[12,13], G. Maier[12], L. Mancini[47,72,73], S. Rahvar[52,70], D. Ricci[54], G. Scarpetta[50], J. Skottfelt[45], J. Southworth[55], J. Surdej[54], and F. Zimmer[12]
(The MiNDSTEp Consortium)[6]

(Affiliations can be found after the references)

Received 6 June 2012 / Accepted 27 August 2012

ABSTRACT

Context. Caustic crossing is the clearest signature of binary lenses in microlensing. In the present context, this signature is diluted by the large source star but a detailed analysis has allowed the companion signal to be extracted.
Aims. MOA 2009-BLG-411 was detected on August 5, 2009 by the MOA-Collaboration. Alerted as a high-magnification event, it was sensitive to planets. Suspected anomalies in the light curve were not confirmed by a real-time model, but further analysis revealed small deviations from a single lens extended source fit.
Methods. Thanks to observations by all the collaborations, this event was well monitored. We first decided to characterize the source star properties by using a more refined method than the classical one: we measure the interstellar absorption along the line of sight in five different passbands (*VIJHK*). Secondly, we model the lightcurve by using the standard technique: make (s, q, α) grids to look for local minima and refine the results by using a downhill method (Markov chain Monte Carlo). Finally, we use a Galactic model to estimate the physical properties of the lens components.
Results. We find that the source star is a giant G star with radius 9 $R_\odot$. The grid search gives two local minima, which correspond to the theoretical degeneracy $s \equiv s^{-1}$. We find that the lens is composed of a brown dwarf secondary of mass $M_S = 0.05\ M_\odot$ orbiting a primary M-star of mass $M_P = 0.18\ M_\odot$. We also reveal a new mass-ratio degeneracy for the central caustics of close binaries.
Conclusions. As far as we are aware, this is the first detection using the microlensing technique of a binary system in our Galaxy composed of an M-star and a brown dwarf.

Key words. binaries: general – gravitational lensing: micro – stars: individual: MOA 2009-BLG-411L

1. Introduction

Gravitational microlensing has now become a robust and efficient way for detecting exoplanets very distant from the Sun that would not be detectable by other methods (Mao & Paczynski 1991; Gould & Loeb 1992; Sumi et al. 2010; Gould et al. 2010; Cassan et al. 2012). Moreover, this technique is uniquely very sensitive to planets orbiting far from their host stars (the majority of planets detected by microlensing are in this range). So, complementary to other techniques, microlensing detections are useful to better understand the planet formation

⋆ Appendix is available in electronic form at http://www.aanda.org
⋆⋆ Royal Society University Research Fellow.

mechanism. Microlensing provides very important statistics of planets around stars in our Galaxy, especially around M dwarfs, which form the majority of lenses (Dominik 2006). Some of them are binaries. It is well known that microlensing is sensitive only to companions orbiting in the "lensing zone" of their host stars, typically beyond the snowline. However, these limits can be extended, as discussed in Han (2009a,b) and Di Stefano (2012). Here, we present the detection of a low mass binary, with a classical $s \equiv s^{-1}$ degeneracy, outside the classical lensing zone. In Sect. 2, we discuss the observations and the method of data reduction. In Sect. 3, we present a refined method for the extraction of the source properties, in particular a better determination of θ_*. Section 4 explains our error bar rescaling method, an important step before binary modelling as discussed in Sect. 5. The mass-ratio degeneracy for close binaries is presented in Sect. 6. Then, we determine the lens properties in Sect. 7 and conclude in Sect. 8.

2. Data sets: observations and data reductions

The MOA-II 1.8 m telescope at Mount John Observatory (New Zealand) issued an alert regarding the Bulge event MOA 2009–BLG–411 ($\alpha = 17^{\rm h}53^{\rm m}58.4^{\rm s}$, $\delta = -29°44'56''$ (J2000.0) and $l = 0.237°$, $b = -1.979°$) on August 5, 2009 (JD =2 455 048.5).

At this time, most telescopes of our networks were still busy with another promising event, MOA 2009–BLG–387, but this new event was bright, so we immediately started to follow it up.

Three nights later it was recognized as a potential high-magnification event so a larger number of telescopes from the various microlensing collaborations (MOA, PLANET, microFUN, RoboNet/LCOGT and MiNDSTEp) began to observe it more intensively. In total, 16 telescopes covered the event in different photometric bands: MOA-I 0.61 m (I-band) and MOA-II 1.8 m (wide MOA-red band) at Mount John (New Zealand), SAAO 1.0 m at Sutherland (South Africa) (V- and I-bands), Canopus 1.0 m at Hobart (Australia) (I-band), Perth/Lowell 0.61 m at Bickley (Australia) (I-band), a fleet of New Zealand amateur telescopes, namely Auckland 0.41 m (R-band), Farm Cove 0.36 m (unfiltered), Molehill 0.30 m (unfiltered), Possum 0.41 m (unfiltered), Bronberg 0.36 m at Pretoria (South Africa) (unfiltered), Wise 0.46 m at Mitzpe Ramon (Israel) (unfiltered), Teide IAC 0.82 m at Canary Islands (I-band), Faulkes North 2.0 m at Haleakala (Hawaii) (SDSS i-band), Faulkes South 2.0 m at Siding Spring (Australia) (SDSS i-band), Liverpool 2.0 m at La Palma (Spain) (SDSS i-band), and Danish 1.5 m at La Silla (Chile) (I-band). Unfortunately CTIO (Chile) was clouded out and could not observe this event.

Thanks to the public availability of data from the different groups, real-time modelling efforts showed that on August 9 the light curve was deviating from a normal Paczyński curve (Paczyński 1986), exhibiting evidence of extended source effects. The event peaked on the same night.

Data reduction was conducted using both point spread function (PSF) photometry based on a customized DoPhot package and image subtraction. The Danish images were reduced with an image subtraction package, namely DIAPL from Pych & Woźniak (Wozniak 2000), which models the convolution kernel for matching a reference image to a target image using a linear combination of a set of Gaussian basis functions of different widths further modified by polynomials, as pioneered by Alard's ISIS package (Alard & Lupton 1998; Alard 2000). RoboNet/LCOGT images were reduced using a different image subtraction package, `DanDIA`, which works by solving for the kernel pixel values directly, imbuing the kernel solution with a flexibility that cannot be matched by the Gaussian expansion (Bramich 2008). PLANET telescopes also use image subtraction: at the telescope an on-line version called WISIS, based on Alard's ISIS package, was used, while version 3.0 of pySIS (Albrow et al. 2009), based on the same numerical kernel as `DanDIA`, was employed for a final reduction. For consistency, we decided to reprocess the RoboNet/LCOGT images using pySIS. MOA images, both from MOA-I and from MOA-II telescopes, were reprocessed using the method described in a previous paper (Bachelet et al. 2012). In the MOA-II images, the target unfortunately falls close to a series of bad columns, which sometimes compromises photometric precision. All μFUN telescope images were first reduced using DoPhot then pySIS.

The final data set, with rejection of outliers, contains 1563 data points from 13 different telescopes (MOA-II: 521 after binning, Auckland R: 57, Farm Cove: 11, Faulkes South i: 299, Faulkes North i:40, SAAO I: 169, SAAO V: 11, Danish I: 30, Liverpool I: 100, Teide I: 50, Wise: 71, MOA-I I: 163, MOA-I V: 41). The lightcurve is shown in Fig. 1.

3. Source properties

The distance to the source and the amount of reddening along the line of sight are uncertainties which always affect the final determination of the properties of the lens-source system, as discussed in detail for instance in Fouqué et al. (2010).

Due to the geometry of the Galactic bulge with a bar embedded in it, the galactic coordinates of the target give an estimate of the relative position of the source with respect to the Galactic centre, if we assume that the source is at the same distance as the majority of the stars in the field. The Galactic centre distance itself is adopted as 8.0 ± 0.5 kpc, given the evolution of the best distance indicator, namely the orbits of stars revolving around the central black hole from $D_{\rm GC} = 7.94 \pm 0.42$ kpc in Eisenhauer et al. (2003) to $D_{\rm GC} = 7.62 \pm 0.32$ kpc in Eisenhauer et al. (2005) and ultimately 8.33 ± 0.35 kpc in Gillessen et al. (2009). The adopted value corresponds to a distance modulus of $\mu_{\rm GC} = 14.52 \pm 0.14$.

We then use Rattenbury et al. (2007), who give the relative positions of the OGLE-II fields with respect to the field BUL_SC45, which contains Baade's Window ($l = 1.00°$ $b = -3.88°$). As assumed by Paczyński & Stanek (1998) and recently confirmed by Nataf et al. (2012), it is probably safe to assume that the mean distance of stars seen in Baade's Window is similar to the Galactic centre distance. Our target's position happens to fall in the OGLE-II field, BUL_SC3, which is claimed to be more distant by 0.07 ± 0.09 mag than BUL_SC45. We therefore adopt as the source distance modulus, $\mu = 14.6 \pm 0.2$.

There are several estimates of the reddening in the $K_{\rm S}$ band at positions near our target. They typically indicate about 0.2 mag of absorption in $K_{\rm S}$. However, given the patchiness of the dust structure, we need an estimate for our target's position. This is based on IRSF/SIRIUS photometry of a $7.7' \times 7.7'$ field containing our target. We use isochrones from Bonatto et al. (2004) based on Padova group models, but directly calibrated for the 2MASS bandpasses. We also calibrated the IRSF/SIRIUS photometry by using the 2MASS stars in the same field to ensure coherence.

We restrict the fitting region to 300 pixels around the target ($2.25' \times 2.25'$) to avoid too much differential extinction. This is large enough to form well-defined colour–magnitude diagrams (CMDs), where the red giant clump (RGC) is easily identified, which is not the case when using only 2MASS because

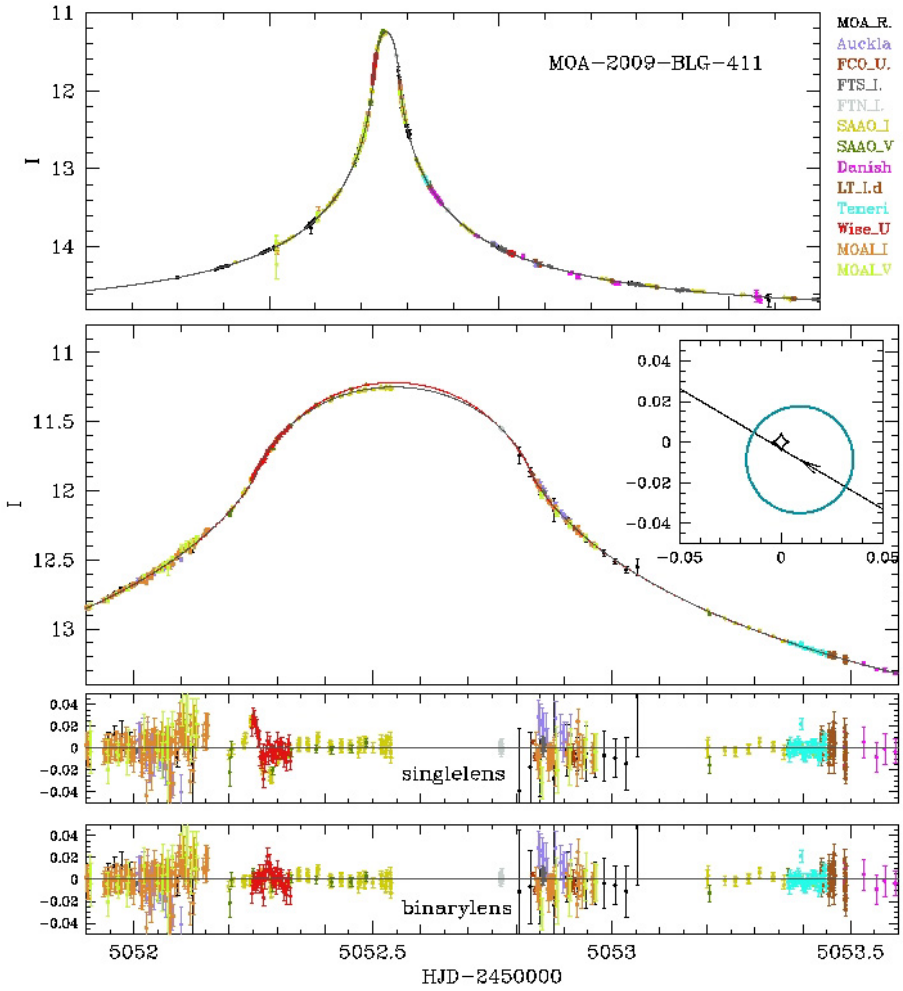

Fig. 1. *Top*: best single lens fit. *Bottom*: zoom close to the peak and residuals for single and best binary lens fits (close model). The geometry of caustic crossing is on the right (see inset), where the source star is represented by the blue circle. Note that the grey curve is for limb-darkening coefficient $\Gamma_\lambda = 0.49$ (R band) and the red curve is for $\Gamma_\lambda = 0.67$ (V band) in the *middle panel*.

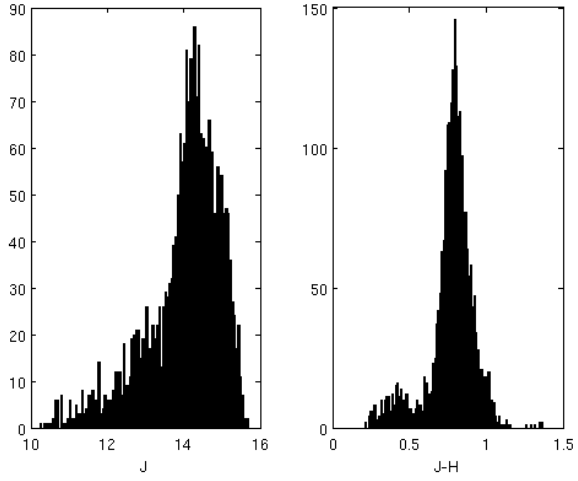

Fig. 2. Histograms of the RGC in J and $J-H$. The colour histogram has a symmetric distribution, while the magnitude histogram is pertubed by the first ascent giant branch.

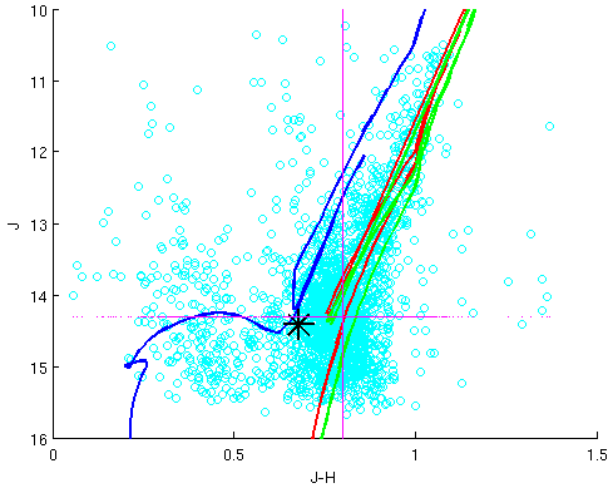

Fig. 3. Colour–magnitude diagram in J and H from IRSF/SIRIUS stars in a $2.25' \times 2.25'$ field around MOA 2009–BLG-411. Superimposed lines are isochrones from Bonatto et al. (2004) for three ages: 0.6 Gyr (blue), 5 Gyr (red), and 10 Gyr (green), assuming solar metallicity, a distance modulus of 14.6, and extinction coefficients of $A_J = 0.57$, $A_H = 0.32$ and $A_{K_s} = 0.19$. The black star symbol marks the position of the source.

its brighter limiting magnitude cuts off part of the clump. As can be seen from Fig. 2 and similar histograms for H and K_s, the mean magnitudes of the RGC are: $J = 14.25$, $H = 13.5$, and $K_s = 13.2$. The corresponding CMD is displayed in Fig. 3.

Although the mean observed magnitude of the clump could in principle give an estimate of its distance, in practice, variations of the absolute magnitudes of clump giants due to a range of ages and metallicities prevent us from deriving an accurate value. Assuming a 10 Gyr isochrone and solar metallicity,

Table 1. Coordinates and magnitudes of the stars close to the target position in 2MASS PSC and IRSF photometric catalogue.

Designation	α (2000)	δ (2000)	J	H	K_s
2MASS 17535841-2944562	17:53:58.41	–29:44:56.2	>13.264	13.042 ± 0.103	>12.315
IRSF	17:53:58.39	–29:44:56.0	14.317 ± 0.042	13.678 ± 0.035	13.486 ± 0.032
IRSF	17:53:58.46	–29:44:57.0	14.402 ± 0.018	13.584 ± 0.016	13.365 ± 0.019

Table 2. Coordinates and magnitudes of the stars close to the target position in MOA and OGLE-III catalogues, and relative shifts in magnitude with respect to the RGC centroid.

Designation	α (2000)	δ (2000)	V	I	I shift	$V-I$ shift
OGLE-III-BLG-101.3 159762	17:53:58.38	–29:44:56.1	17.927 ± 0.021	15.813 ± 0.015	–0.127	–0.271
OGLE-III-BLG-101.3 160107	17:53:58.46	–29:44:57.0	18.220 ± 0.026	15.947 ± 0.010	0.007	–0.112
OGLE-III-BLG-101.3 160108	17:53:58.44	–29:44:55.1	18.024 ± 0.026	16.536 ± 0.023	0.596	–0.897
MOA 2009–BLG–411	17:53:58.40	–29:44:56.01				

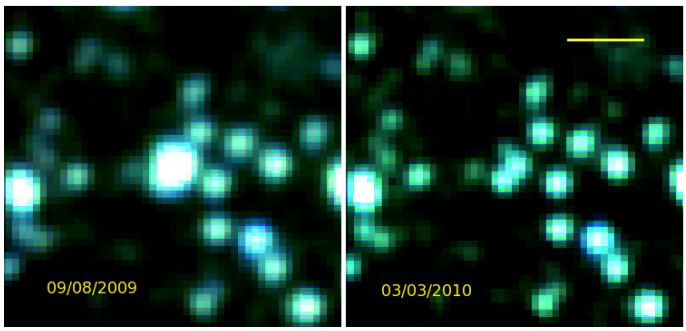

Fig. 4. A comparison of 2009 and 2010 observations at IRSF around the target position. North is up and east on the left side, and the horizontal line corresponds to 5 arcsec. The amplification of the source is obvious in the 2009 frame, while two stars are clearly separated in the 2010 frame: the westernmost star at the centre of the chart is our target. A third faint component north of the two other stars is also visible.

we get the following estimates of the near-infrared extinction and reddening law:

$$A_{K_s} = 0.19 \quad (1)$$

$$A_H = 1.7 \times A_{K_s} = 0.32 \quad (2)$$

$$A_J = 3.0 \times A_{K_s} = 0.57. \quad (3)$$

These value are in good agreement with the reddening law of Nishiyama et al. (2009) and our value for $E(J-K)$ (0.38) confirmed the extinction measured by the VVV telescope based in Chile (0.39) (Gonzalez et al. 2012). The PSF photometry obtained from IRSF images reveals two components at the target position. At the time when the images were taken (JD = 2 445 053.33929), the amplification of the source was 13.7 according to our model. So we have to add 2.842 mag to the IRSF measurements to find the unamplified magnitude of the source in each band. This magnitude shift is the same in all bands, as gravitational microlensing is an achromatic effect, except for the differential limb-darkening correction due to extended source effects, which are negligible in the near-infrared bands. However, the deblending of the two components may not be perfect, due to the huge amplification of the source at that time.

For this reason, a new set of images was taken at the IRSF as soon as the target became visible in 2010, namely on March 3. A comparison of the two observations clearly illustrates the microlensing amplification, as can be seen in Fig. 4. On the 2010 image, two stars are clearly separated, our target being the westernmost component. A third faint star can be seen north of the other two, but it is not separated by DAOFIND in the final catalogue. In the following, we use the photometry from the 2010 observations, avoiding the need to correct for amplification and inaccurate deblending.

The target is also listed in the 2MASS PSC catalogue. However its photometry is rather imprecise, J and K_s being upper limits and H having a 0.1 mag uncertainty. This probably comes from the fact that the 2MASS "star" is in fact a blend of 3 stars. The accurate coordinates and magnitudes of the various objects at this position are given in Table 2 for OGLE and MOA, and in Table 1 for 2MASS and IRSF.

Although the 2MASS flags do not indicate any blending, the coordinates and magnitudes correspond well to the blend of the two IRSF stars. The microlensed source is the western component and the other IRSF star is a blend of the two other OGLE-III stars. However, as one of these stars is clearly bluer than the other, only the red one actually contributes to the near-infrared flux.

After converting IRSF magnitudes to the 2MASS photometric system using Kato et al. (2007), we get for the near-infrared magnitudes of the source: $J = 14.328$, $H = 13.644$ and $K_s = 13.463$. After correcting for our adopted values of absorption, this becomes $J_\circ = 13.76$, $H_\circ = 13.32$, and $K_{s\circ} = 13.27$. Finally, converting to the standard Bessell & Brett photometric system (Bessell & Brett 1988) using the revised version of the conversion equations originally published in Carpenter (2001), as given in the on-line version of the Explanatory Supplement to 2MASS[1], we get $K_\circ = 13.31$ and $(J-K)_\circ = 0.52$. Using $V_\circ = 15.2$ as derived in the Appendix, we get $(V-K)_\circ = 1.9$.

From the adopted dereddened magnitudes and colours, and using the surface brightness – colour relations in $K_\circ$, $(V-K)_\circ$ published by Groenewegen (2004), we get an estimate of the angular source radius θ_* in μas of

$$\log \theta_* = -0.2K_\circ + 0.045(V-K)_\circ + 3.283. \quad (4)$$

The uncertainty of this estimate is 0.024, so adding quadratically the uncertainty in the magnitude (0.1) and estimated colour (0.07) gives an accuracy of 7% on θ_*, i.e., $\theta_* = 4.8 \pm 0.3$ μas. At the adopted source distance, this translates into a linear radius of $R_* = 9\ R_\odot$, typical of a G giant.

We repeated this procedure for the visible CMD, as reported in the appendix.

[1] http://www.ipac.caltech.edu/2mass/releases/allsky/doc/sec6_4b.html

Using the dereddened colours and, for instance, the Houdashelt et al. (2000) tables, we estimate the effective temperature of the source star to be about 5250 K and the bolometric correction in K to be 1.7. Looking at Marigo et al. (2008) isochrones for a model star with similar characteristics to ours, our fits always tend to a star aged about 1.0 Gyr for solar metallicity, in other words, a giant of 2.1 $M_\odot$ and $\log g = 3.0$ on the first ascent giant branch. These are the blue isochrones in both Figs. 3 and A.2. This is very young for a Bulge star but Bensby et al. (2011) show that the age dispersion is large (1 to 13 Gyr) in the Bulge population. The star is clearly on the edge of this range but could support these previous observations. Another explanation is that the source star belongs to the disk of the Galaxy, which contains younger stars. A future high-resolution spectroscopic study would be useful to accurately measure $T_{\rm eff}$, $\log g$ and metallicity and see which scenario is preferred.

4. Data analysis: a noise model

From the original data set, we remove MOA data points earlier than HJD′ = 4850 (HJD′ = HJD-2 450 000). This corresponds to selecting only the 2009 observing season. We also binned the data outside of the peak. The reason for this cut is twofold: the planetary deviation search is very demanding in terms of CPU time, so reducing the number of points helps; moreover, the number of data points in the baseline before HJD′ = 4850 is quite large, and any slight error in the photometric error estimate may bias the fit. We verified that this does not change the resulting fit parameters. We proceed to rescale photometric error bars in a consistent way. We first find a good single lens fit without rescaling. Then, we rescale error bars for this model. We avoid the classical approach (decrease the χ^2/d.o.f. to one for each data set) which generally increases the error bars too much and, for our event, hides the caustic perturbation. We use two parameters (f, the classical rescaling factor and a minimal error $e_{\rm min}$ which can reproduce the dispersion at high magnification) for rescaling as follows:

$$e = f\sqrt{e_{\rm ori}^2 + e_{\rm min}^2}. \quad (5)$$

We adjust those parameters as in Appendix C of Bachelet et al. (2012) and in Miyake et al. (2012) by using a standard cumulative distribution for Gaussian errors. If the dispersion of data is well represented by the original error bars, we set $f = 1$ and $e_{\rm min} = 0$. After some iteration, we find good pairs of parameters for each telescope and we keep them for the next step of the modelling. Results are shown in Table 3. We do not apply this procedure to data sets with fewer than ∼30 points to ensure meaningful statistical results.

Table 3. Adopted error rescaling and limb-darkening parameters.

Telescope	Ndata	Binning	Γ_λ	f	$e_{\rm min}$
MOA II_R	521	Yes	0.4979	2.3	0.001
Auckland	57	No	0.454	0.8	0.02
FCO	11	No	0.4979	1.0	0.0
FTS	299	No	0.454	1.59	0.0
FTN	40	No	0.454	1.0	0.002
SAAO_I	169	No	0.454	4.7	0.0
SAAO_V	11	No	0.6798	4.1	0.0
Danish	30	No	0.454	5.4	0.0
LT	100	No	0.454	1.2	0.008
Teide	50	No	0.454	4.0	0.0
Wise	71	No	0.4979	1.2	0.006
MOA I_I	163	No	0.454	1.3	0.005
MOA I_V	41	No	0.6798	1.1	0.001

5. Modelling

At first glance, this event looks like a single lens passing close enough to the source star to produce strong finite source effects in the lightcurve. We first perform a single-lens fit by using four single-lens parameters, namely $t_{\rm E}$, the Einstein time scale, $u_\circ$, the lens-source minimal separation, $t_\circ$, the corresponding time, and, to take account of finite source effects, the normalized angular source radius ρ_*. Our best single-lens fit gave $\chi^2 = 2156.21$ for 1563 data points and was unable to explain the deviations at peak, as we can see in Fig. 1. Different phenomena could explain these residuals: the presence of a companion, inadequate limb-darkening treatment or stellar variability. Two arguments suggest that the binary lens is the most reasonable solution. As previously emphasised by Dong et al. (2009), it is well known that gravitational lensing is achromatic. The residuals close to the peak have the same shape and amplitude in both SAAO-I and SAAO-V, showing the phenomenon was achromatic. The presence of anomalies only close to the peak, and their relative symmetry about it, rationally exclude stellar variability. Nevertheless, anomalies are clearly low amplitude for microlensing. A similar phenomenon has already been treated by Dong et al. (2009) and Janczak et al. (2010), who explain it as due to the low value of w/ρ_* (comparable to or less than two), with w the "width" of the central caustic (Chung et al. 2005; Dong et al. 2009), which means that only a fraction of the source star is magnified by the caustic during the peak. As can be seen in Table 4, our single-lens parameter $u_\circ$ is small enough to ensure that we pass close to the central caustic, if it exists, and ρ_* (see below) has a larger value than is typical for microlensing. All these considerations strongly suggest we have here a case as described above: a binary lens crossing a giant source. Then, we decided to investigate binary models by using the four parameters above and the three classical binary parameters: s, the projected separation between the two components in units of the Einstein radius, q, the mass ratio and α, the angle between the trajectory of the source and the binary axis. By convention, we define q as the mass ratio of the rightmost component over the leftmost one; therefore, q may take values larger than one.

Our exploration of parameter space first uses (q, s, α) grids to look for all minima in χ^2 space. We use a Markov chain Monte Carlo (MCMC) algorithm for each pair of grid parameters to find the best solution for the other parameters. We start with a very large range for each parameter: 10^{-2} to 10 for s, 10^{-4} to 1 for q and 0 to 2π for α to explore all possible minima. We accelerate the calculation by using the "map making" technique first introduced by Dong et al. (2006) for the region close to the caustics and a Taylor development of source magnification, known as a "hexadecapole approximation" (Gould 2008; Pejcha & Heyrovský 2009), for more distant regions. We take account of the limb darkening by using a linear approximation, sufficient in our case, following Milne's description (Milne 1921; An et al. 2002):

$$I_\lambda = \frac{F_\lambda}{\pi\theta_*^2}\left[1 - \Gamma_\lambda\left(1 - \frac{3}{2}\cos\phi\right)\right] \quad (6)$$

where Γ_λ is the limb-darkening coefficient at wavelength λ, which is different for all telescopes, F_λ is the total flux from the star and ϕ is the angle between the line of sight and the normal to the stellar surface. The value of Γ_λ for each telescope

Table 4. Parameters for close and wide models.

Parameters	Single lens	Close	Wide
$t_\circ$ (days)	5052.5446	5052.5439 ± 0.0003	5052.5437 ± 0.0004
$u_\circ$	0.00041	0.0029 ± 0.0005	0.0018 ± 0.0007
t_E (days)	10.76	10.71 ± 0.1	15.06 ± 1.9
ρ_*	0.027	0.026 ± 0.0003	0.019 ± 0.0026
s		0.115 ± 0.013	14.5 ± 2.61
q		3.74 ± 0.38	0.99 ± 0.29
α		3.67 ± 0.07	0.547 ± 0.06
$\chi 2$	2156.21	1578.513	1586.947

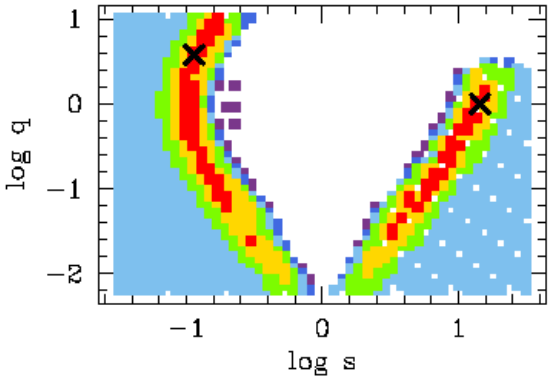

Fig. 5. χ^2 landscape of mass ratio versus lens separation. Red, yellow, green, cyan, blue and purple colours show the one to six sigma regions away from the best model. The two crosses mark the positions of the final best fit models for the close and wide solutions.

(see Table 3) was found by an initial extended source single-lens fit with free limb-darkening coefficients for each colour. The resulting values are in good agreement with coefficients given in Claret (2000) for a giant star with an effective temperature of 5250 K and $\log g = 3.0$.

Finally, we found two local minima which correspond to the classical degeneracy of $s \equiv s^{-1}$, as can be seen in Fig. 5. We investigated both, by using a MCMC algorithm for all parameters, to find the model parameters listed in Table 4 and the model lightcurves in Fig. 1.

6. Study of deviations due to caustic crossing

Adding a companion to the lens greatly improves the fit. We find for both models that the ratio w/ρ_* is smaller than two (in our case ∼0.3), which indicates that the source star "smoothed" the light curve deviation induced by the caustic crossing near the peak. The same central caustic can be created by a close companion or a distant companion; this is the close/wide degeneracy (i.e., $s \equiv s^{-1}$). Both cases were explored. It is well known that microlensing is sensitive to companions orbiting in the "lensing zone" of their host, i.e., $s \in [0.6, 1.6]$. The majority of detected events are in this range but there can be exceptions. Griest & Safizadeh (1998) first showed that detection of companions with appropriate mass ratios and $u_\circ$ values is possible for $s = 0.2$. More recently, Han (2009a,b) and Han & Kim (2009) went into further details, especially for giant source stars. For a w/ρ_* ratio close to 0.5, it is shown that the limits of the "lensing zone" become

$$\sqrt{\frac{2q}{\rho_*}+1}-\sqrt{\frac{2q}{\rho_*}} \le s \le \sqrt{\frac{2q}{\rho_*}+1}+\sqrt{\frac{2q}{\rho_*}}. \quad (7)$$

In our case, for $q \equiv 1$ and $\rho_* \equiv 0.025$, our values $s_{\rm close} = 0.11$ and $s_{\rm wide} = 14.5$ are in the range predicted above [0.056−17.9]. Nevertheless, experimental detection can be difficult because the magnification excess over a single-lens model can be as low as 5% (Han & Kim 2009). Our central caustic looks symmetric (diamond shape) and our models are degenerate modulo $\frac{\pi}{2}$. The excess magnification for this kind of caustic (see Han 2009a) is also symmetric with respect to a rotation of $\frac{\pi}{2}$. However, the angle of the trajectory is not a "physical" parameter and we always find for these four values of α similar values for s and q as those given in Table 4. The theoretical anomalies predicted by Han (2009a) for a diamond-shaped central caustic are similar to ours (see his Fig. 3) and we can conclude that we have made the first experimental detection of this predicted effect. Figure 6 shows our MCMC exploration around our two best fit models. We can see a parabolic degeneracy in $\log q$ versus s for the close case. Following Chung et al. (2005), we did some algebra based on theory developed by An (2005), and found that the central caustic position is given by the following complex coordinate:

$$\zeta_c = \frac{|C_1|}{2}\left(e^{3i\phi}+3e^{-i\phi}\right)+|C_2|\left(e^{4i\phi}+2e^{-2i\phi}\right). \quad (8)$$

This gives the following Cartesian coordinates:

$$\xi_c = 2\,|C_1|\cos(\phi)^3+3\,|C_2|\left(2\cos(\phi)^4-1\right) \quad (9)$$

$$\eta_c = -2\,|C_1|\sin(\phi)^3-8\,|C_2|\sin(\phi)^3\cos(\phi) \quad (10)$$

with

$$C_{1\rm close} = \frac{qs^2}{(1+q)^2} \qquad C_{1\rm wide} = \frac{q}{(1+q)s^2} \quad (11)$$

$$C_{2\rm close} = C_{1\rm close}\frac{(1-q)s}{(1+q)} \qquad C_{2\rm wide} = \frac{C_{1\rm wide}}{\sqrt{(1+q)s}}. \quad (12)$$

(See Fig. 7 for the meaning of these variables.)

The cusps are for values of ϕ which are solutions of $\frac{d\zeta_c}{d\phi} = 0$. They occur for $\phi = 0$, $\frac{\pi}{2}$, π and $\frac{3\pi}{2}$. Knowing that, we now define the horizontal and vertical width as Chung et al. (2005) and find

$$\Delta\xi_c = \Delta\eta_c = 4\,|C_1| \quad (13)$$

which leads to

$$\Delta\eta_c = 4\frac{qs^2}{(1+q)^2} \quad (14)$$

for the close case and

$$\Delta\eta_c = 4\frac{q}{(1+q)s^2} \quad (15)$$

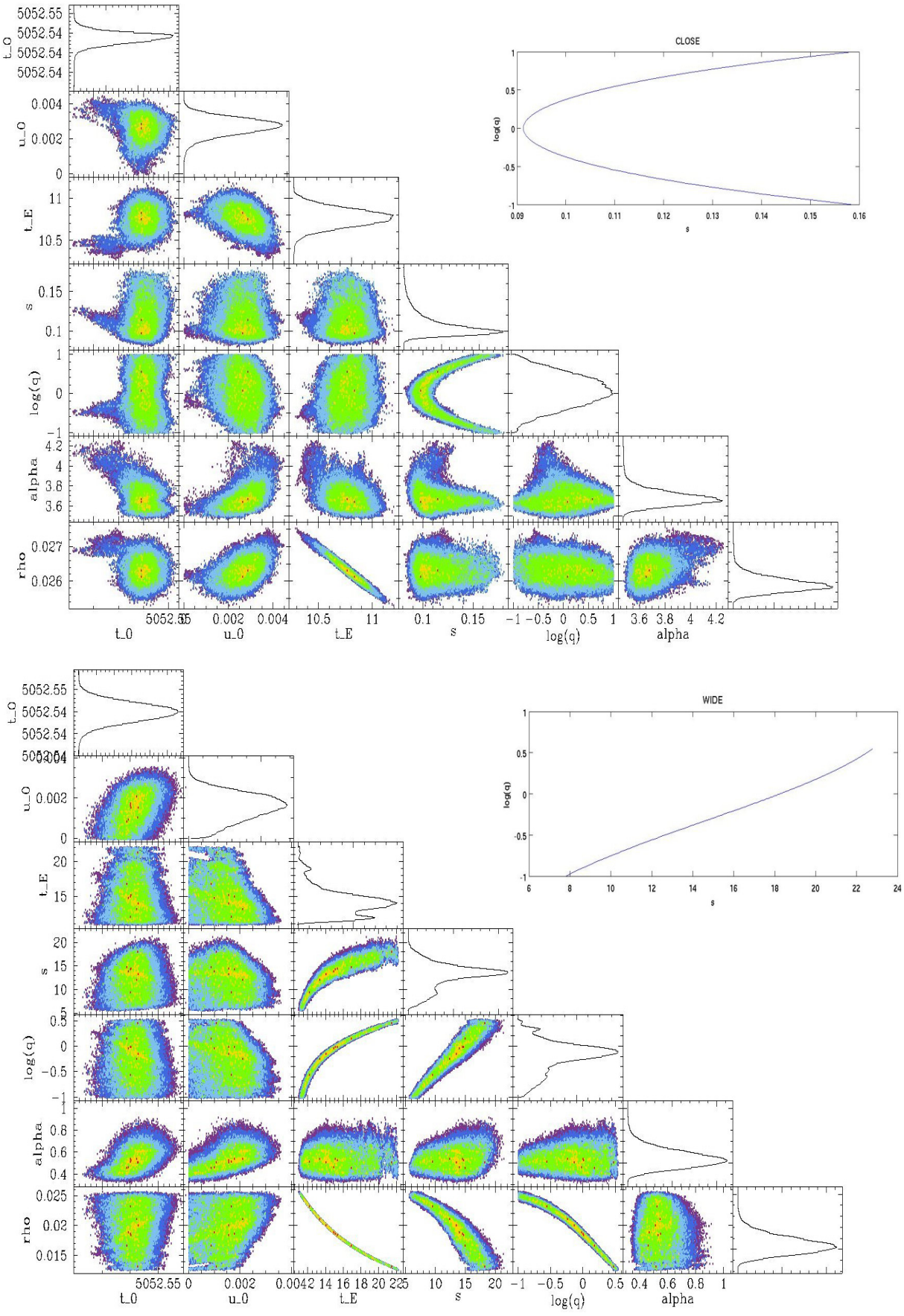

Fig. 6. Scatter plots for our best models. The close model exploration is on the top and the wide one on bottom. For both case, the theoritical plot of Eq. (16) is visible on the right. The log q versus s parabolic degeneracy is cleary visible for the close model.

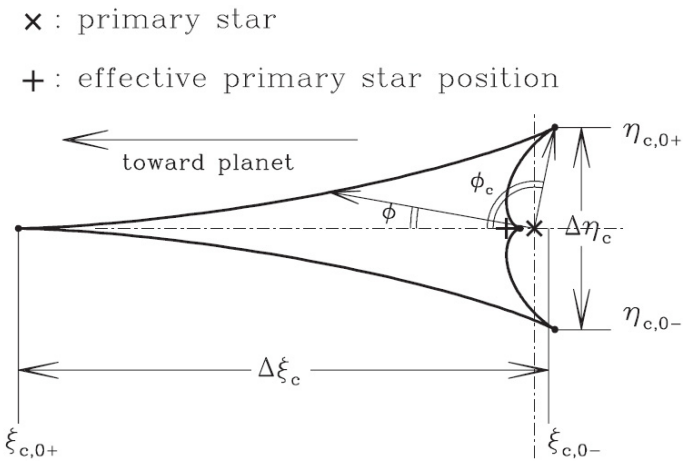

Fig. 7. Geometry of central caustic (from Chung et al. 2005).

for the wide case. This gives a width ratio $R_c = 1$, in perfect agreement with our experimental "diamond-shaped" central caustic for both cases. Then, we consider our experimental case with $w \equiv \frac{\rho_*}{3}$ which gives

$$s_{\rm close} = \sqrt{\frac{\rho_*(1+q)^2}{12q}} \qquad s_{\rm wide} = \sqrt{\frac{12q}{\rho_*(1+q)}}. \tag{16}$$

Our theoretical plot of Eq. (16) can be seen in Fig. 6. These relations are in excellent agreement with our experimental results (MCMC search). We also checked its validity for a few other events (Choi et al. 2012). We conclude that, as far as we know, we have uncovered a new central caustic degeneracy, in terms of q, for extremely close binaries. This degeneracy is however not dramatic for microlensing studies in terms of physical parameters (lens mass and component separation), as is the case with the $s \equiv s^{-1}$ degeneracy. Because of the near-exact symmetry of excess magnification (see Fig. 2 in Han 2009a), close models cannot be distinguished if the source passes the most massive component of the lens on its right/left, which explains the $q \equiv q^{-1}$ degeneracy (see definition of q in Sect. 5). For wide models, this symmetry exists close to the central caustic, but the degeneracy is broken by the presence of the larger planetary caustic.

7. Results

In principle, a measurement of the source size in both Einstein radius and physical units, as well as the measurement of parallax parameters completely determines the lens location (given the source distance D_S). As indicated before, standard models are not well enough constrained, so that modelling second-order effects (microlensing parallax, xallarap, or/and orbital motion), which will add more degeneracy, is clearly not possible and, more important, not reliable. Moreover, this event is of very short duration, so we can expect that these effects are quite small and, in practice, not measurable. That is why we did not explore this kind of modelling for this event.

With the angular Einstein radius being related to the angular source radius θ_* as $\theta_E = \theta_*/\rho_*$, we find $\theta_E = 185 \pm 20\,\mu$as for the close model. This value is lower than for typical microlensing events. This means that the lens is probably close to the Galactic bulge with a low mass. This enables us to calculate the relative lens-source proper motion, $\mu_{\rm rel} = \theta_E/t_E = 6.3 \pm 0.4$ mas/yr. From

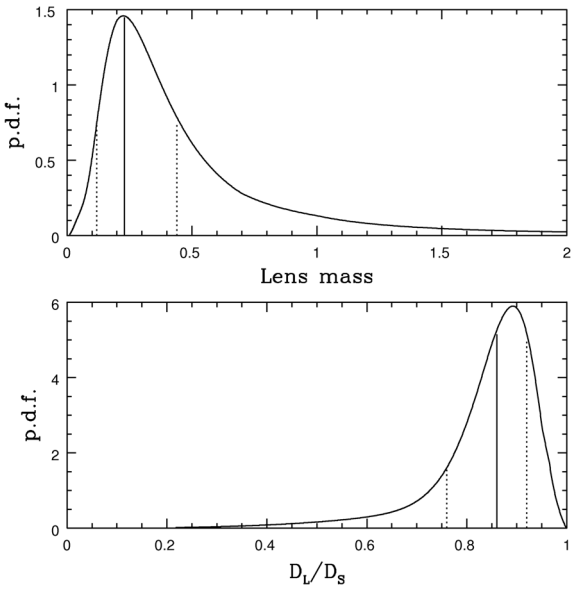

Fig. 8. Probability densities for the lens mass $\frac{M_L}{M_\odot}$ and the lens distance D_L for the adopted Galaxy model and the close configuration. Vertical lines correspond to the median, and the first and last quartiles (dashed).

the value of θ_E in mas and D_S in kpc, we obtain a constraint on the lens mass M_L in solar mass units as follows (Dominik 1998):

$$M_L(x) = \frac{\theta_E^2 D_S}{8.144}\frac{x}{1-x} \tag{17}$$

where $x = \frac{D_L}{D_S}$, which for $D_S = 8.5$ kpc and $\theta_E = 0.185$ mas gives

$$M_L(x) = 0.036\frac{x}{1-x}M_\odot. \tag{18}$$

We then use estimates of the physical parameters, following Dominik (2006) and assuming his adopted Galaxy model. For the close model, the event time-scale, $t_E = 10.7$ days, and the angular Einstein radius, $\theta_E = 0.185$ mas, provide us probability densities for the lens mass M_L and lens distance D_L as seen in Fig. 8. We find a median lens mass $M_L = 0.23^{+0.21}_{-0.11}\,M_\odot$ and distance $D_L = 7.3^{+0.5}_{-0.9}$ kpc. The wide model leads to similar values, $M_L = 0.32^{+0.29}_{-0.15}\,M_\odot$ and $D_L = 7.0^{+0.6}_{-1.0}$ kpc.

8. Summary and conclusion

Dense photometric coverage made by all observational teams permitted a detailed study of MOA-2009-BLG-411. The maximum magnification was about $A_{\rm max} \equiv 80$ and so was very sensitive to the presence of a central caustic. A caustic crossing signature did not appear clearly, because of a large normalized source radius ρ_*, but we found that considering a binary geometry increases the quality of the fit substantially. After exploration of the two local minima ($s \equiv s^{-1}$ degeneracy), we found that the close model gives a slightly better fit. The model was highly degenerate for two major reasons: the peak was not sufficiently monitored and the theoretical degeneracy in q allows a large range of s values. Our study of the red giant clump, which gives a better estimation of extinction, leads to a source radius $\theta_* = 4.8 \pm 0.4\,\mu$as and so an Einstein ring radius $\theta_E = 0.185$ mas. Finally, our Galactic and microlensing models lead to a binary system with an M-dwarf with mass, $M_P = 0.18\,M_\odot$, and a brown dwarf with mass, $M_S = 0.05\,M_\odot$, separated by a projected distance 0.15 AU (close model). This result is a new example of

a brown dwarf in orbit around an M-dwarf, following the first results of Marley et al. (1996) and more recently of Irwin et al. (2010) and Johnson et al. (2011), based on transit-survey data.

Acknowledgements. We are very grateful to the observatories that support our science (Bronberg, Canopus, CTIO, ESO, IRSF, LCOGT, Liverpool, LOAO, MOA, OGLE, Perth, SAAO, Skinakas) via the generous allocation of time that makes this work possible. The operation of Canopus Observatory is in part supported by a financial contribution from David Warren. Allocation of the Holmes grant from the French Agence Nationale de la Recherche has been indispensable to finance observing trips and travel costs for meetings, and is gratefully acknowledged here. D.H. was supported by Czech Science Foundation grant GACR 205/07/0824 and by the Czech Ministry of Education project MSM0021620860. C.H. was supported by the grant 2009-0081561 of National Research Foundation of Korea. T.C.H. was financed for his astronomical research at the Armagh Observatory by the Department for Culture, Arts and Leisure, Northern Ireland, UK and is now supported by the Korea Research Council for Fundamental Science and Technology (KRCF) via the Young Scientist Research Fellowship Program. MOA project was funded by JSPS18253002 and JSPS20340052. T.S. was funded by JSPS20740104. D.R. and J.S. acknowledge support from the Communauté française de Belgique – Actions de recherche concertées – Académie universitaire Wallonie-Europe. P.F. wishes to thank Noriyuki Matsunaga for discussions about the interplay between adopted distance and derived extinction. The research leading to these results has received funding from the European Community's Seventh Framework Programme (/FP7/2007-2013/) under grant agreement No 229517. A. Gould acknowledges support from NSF AST-1103471. B. S. Gaudi, A. Gould, and R. W. Pogge acknowledge support from NASA grant NNG04GL51G. Work by J. C. Yee is supported by a National Science Foundation Graduate Research Fellowship under Grant No. 2009068160. Work by S. Dong was performed under contract with the California Institute of Technology (Caltech) funded by NASA through the Sagan Fellowship Program. The RoboNet team is supported by the Qatar Foundation through QNRF grant NPRP-09-476-1-78. CUL acknowledges support by Korea Astronomy and Space Science Institute (KASI) grant 2012-1-410-02. This publication makes use of data products from the 2MASS project, as well as the SIMBAD database, Aladin and Vizier catalogue operation tools (CDS Strasbourg, France). The Two Micron All Sky Survey is a joint project of the University of Massachusetts and the Infrared Processing and Analysis Center/California Institute of Technology, funded by the National Aeronautics and Space Administration and the National Science Foundation. This work was granted access to the HPC resources of CALMIP under the allocation 2012-[1131].

References

Alard, C. 2000, A&AS, 144, 363
Alard, C., & Lupton, R. H. 1998, ApJ, 503, 325
Albrow, M. D., Horne, K., Bramich, D. M., et al. 2009, MNRAS, 397, 2099
An, J. H. 2005, MNRAS, 356, 1409
An, J. H., Albrow, M. D., Beaulieu, J.-P., et al. 2002, ApJ, 572, 521
Bachelet, E., Shin, I.-G., Han, C., et al. 2012, ApJ, 754, 73
Bensby, T., Adén, D., Meléndez, J., et al. 2011, A&A, 533, A134
Bessell, M. S., & Brett, J. M. 1988, PASP, 100, 1134
Bonatto, C., Bica, E., & Girardi, L. 2004, A&A, 415, 571
Bramich, D. M. 2008, MNRAS, 386, L77
Carpenter, J. M. 2001, AJ, 121, 2851
Cassan, A., Kubas, D., Beaulieu, J.-P., et al. 2012, Nature, 481, 167
Choi, J.-Y., Shin, I.-G., Han, C., et al. 2012, ApJ, 756, 48
Chung, S.-J., Han, C., Park, B.-G., et al. 2005, ApJ, 630, 535
Claret, A. 2000, A&A, 363, 1081
Di Stefano, R. 2012, ApJ, 752, 105
Dominik, M. 1998, A&A, 329, 361
Dominik, M. 2006, MNRAS, 367, 669
Dong, S., DePoy, D. L., Gaudi, B. S., et al. 2006, ApJ, 642, 842
Dong, S., Bond, I. A., Gould, A., et al. 2009, ApJ, 698, 1826
Eisenhauer, F., Schödel, R., Genzel, R., et al. 2003, ApJ, 597, L121
Eisenhauer, F., Genzel, R., Alexander, T., et al. 2005, ApJ, 628, 246
Fouqué, P., Heyrovský, D., Dong, S., et al. 2010, A&A, 518, A51
Gillessen, S., Eisenhauer, F., Trippe, S., et al. 2009, ApJ, 692, 1075
Girardi, L., & Salaris, M. 2001, MNRAS, 323, 109
Gonzalez, O. A., Rejkuba, M., Zoccali, M., et al. 2012, A&A, 543, A13
Gould, A. 2008, ApJ, 681, 1593
Gould, A., & Loeb, A. 1992, ApJ, 396, 104
Gould, A., Dong, S., Gaudi, B. S., et al. 2010, ApJ, 720, 1073
Griest, K., & Safizadeh, N. 1998, ApJ, 500, 37
Groenewegen, M. A. T. 2004, MNRAS, 353, 903
Han, C. 2009a, ApJ, 691, L9
Han, C. 2009b, ApJ, 691, 452
Han, C., & Kim, D. 2009, ApJ, 693, 1835
Houdashelt, M. L., Bell, R. A., & Sweigart, A. V. 2000, AJ, 119, 1448
Irwin, J., Buchhave, L., Berta, Z. K., et al. 2010, ApJ, 718, 1353
Janczak, J., Fukui, A., Dong, S., et al. 2010, ApJ, 711, 731
Johnson, J. A., Apps, K., Gazak, J. Z., et al. 2011, ApJ, 730, 79
Kato, D., Nagashima, C., Nagayama, T., et al. 2007, PASJ, 59, 615
Kervella, P., & Fouqué, P. 2008, A&A, 491, 855
Mao, S., & Paczynski, B. 1991, ApJ, 374, L37
Marigo, P., Girardi, L., Bressan, A., et al. 2008, A&A, 482, 883
Marley, M. S., Saumon, D., Guillot, T., et al. 1996, Science, 272, 1919
Milne, E. A. 1921, MNRAS, 81, 361
Miyake, N., Udalski, A., Sumi, T., et al. 2012, ApJ, 752, 82
Nataf, D. M., Gould, A., Fouqué, P., et al. 2012 [arXiv:1208.1263]
Nishiyama, S., Tamura, M., Hatano, H., et al. 2009, ApJ, 696, 1407
Paczyński, B. 1986, ApJ, 304, 1
Paczyński, B., & Stanek, K. Z. 1998, ApJ, 494, L219
Pejcha, O., & Heyrovský, D. 2009, ApJ, 690, 1772
Rattenbury, N. J., Mao, S., Sumi, T., et al. 2007, MNRAS, 378, 1064
Salaris, M., & Girardi, L. 2002, MNRAS, 337, 332
Sumi, T. 2004, MNRAS, 349, 193
Sumi, T., Bennett, D. P., Bond, I. A., et al. 2010, ApJ, 710, 1641
Szymański, M. K., Udalski, A., Soszyński, I., et al. 2011, Acta Astron., 61, 83
Udalski, A. 2003, ApJ, 590, 284
Wozniak, P. R. 2000, Acta Astron., 50, 421

[1] Probing Lensing Anomalies Network, http://planet.iap.fr
[2] Microlensing Follow Up Network, http://www.astronomy.ohio-state.edu/~microfun
[3] The Optical Gravitational Lensing Experiment, http://ogle.astrouw.edu.pl
[4] Microlensing Observations in Astrophysics, http://www.phys.canterbury.ac.nz/moa
[5] Robotic Telescope Network, http://robonet.lcogt.net
[6] Microlensing Network for the Detection of Small Terrestrial Exoplanets, http://www.mindstep-science.org
[7] Department of Astronomy, Ohio State University, 140 West 18th Avenue, Columbus, OH 43210, USA
[8] University of Canterbury, Department of Physics & Astronomy, Private Bag 4800, Christchurch 8020, New Zealand
[9] European Southern Observatory (ESO), Casilla 19001, Vitacura 19, Santiago, Chile
[10] European Southern Observatory, Karl-Schwarzschild-Straβe 2, 85748 Garching bei München, Germany
[11] Institut d'Astrophysique de Paris, CNRS, Université Pierre & Marie Curie, 98bis Bd Arago, 75014 Paris, France
[12] Astronomisches Rechen-Institut (ARI), Zentrum für Astronomie der Universität Heidelberg (ZAH), Mönchhofstrasse 12ŋ-14, 69120 Heidelberg, Germany
[13] Scottish Universities Physics Alliance, School of Physics & Astronomy, University of St Andrews, North Haugh, St Andrews, KY16 9SS, UK
[14] University of Notre Dame, Department of Physics, 225 Nieuwland Science Hall, Notre Dame, IN 46556, USA
[15] University of Texas, McDonald Observatory, 16120 St Hwy Spur 78, Fort Davis TX 79734, USA
[16] Institute of Geophysics and Planetary Physics (IGPP), L-413, Lawrence Livermore National Laboratory, PO Box 808, Livermore, CA 94551, USA
[17] Physics Department, Faculty of Arts and Sciences, University of Rijeka, Omladinska 14, 51000 Rijeka, Croatia
[18] Technical University of Vienna, Dept. of Computing, Wiedner Hauptstrasse 10, Vienna, Austria
[19] School of Mathematics and Physics, University of Tasmania, Private Bag 37, Hobart, 7001 Tasmania, Australia
[20] NASA Exoplanet Science Institute, Caltech, MS 100-22, 770 South Wilson Avenue, Pasadena, CA 91125, USA
[21] Perth Observatory, Walnut Road, Bickley, Perth 6076, Australia
[22] South African Astronomical Observatory, PO Box 9, 7925 Observatory, South Africa

[23] Space Telescope Science Institute, 3700 San Martin Drive, Baltimore, MD 21218, USA
[24] Department of Physics, Institute for Basic Science Research, Chungbuk National University, 361-763 Chongju, Korea
[25] Korea Astronomy and Space Science Institute, 61-1, Whaam-Dong, Youseong-Gu, 305-348 Daejeon, Korea
[26] Bronberg Observatory, Pretoria, South Africa
[27] Warsaw University Observatory. Al. Ujazdowskie 4, 00-478 Warszawa, Poland
[28] Universidad de Concepción, Departamento de Física, Astronomy Group, Casilla 160-C, Concepción, Chile
[29] Institute of Astronomy, University of Cambridge, Madingley Road, Cambridge CB3 0HA, UK
[30] Institute of Information and Mathematical Sciences, Massey University, Private Bag 102-904, North Shore Mail Centre, Auckland, New Zealand
[31] Department of Earth and Space Science, Osaka University, 560-0043 Osaka, Japan
[32] Jodrell Bank Centre for Astrophysics, University of Manchester, Manchester M13 9PL, UK
[33] Department of Physics, Konan University, Nishiokamoto 8-9-1, 658-8501 Kobe, Japan
[34] Nagano National College of Technology, 381-8550 Nagano, Japan
[35] Department of Physics, University of Auckland, Private Bag 92019, 1142 Auckland, New Zealand
[36] Tokyo Metropolitan College of Industrial Technology, 116-0003 Tokyo, Japan
[37] Department of Physics and Astrophysics, Faculty of Science, Nagoya University, 464-8602 Nagoya, Japan
[38] Mount John Observatory, PO Box 56, 8770 Lake Tekapo, New Zealand
[39] Las Cumbres Observatory, 6740B Cortona Dr, suite 102, Goleta, CA 93117, USA
[40] Astrophysics Research Institute, Liverpool John Moores University, Twelve Quays House, Egerton Wharf, Birkenhead CH41 1LD, UK
[41] School of Physics, University of Exeter, Stocker Road, Exeter EX4 4QL, UK
[42] Department of Physics, University of Warwick, Coventry, CV4 7AL, UK
[43] Department of Physics, Broida Hall, University of California, Santa Barbara CA 93106-9530, USA
[44] IRAP, Université de Toulouse, CNRS, 14 avenue Edouard Belin, 31400 Toulouse, France
[45] Niels Bohr Institute and Centre for Star and Planet Formation, University of Copenhagen, Juliane Maries Vej 30, 2100 Copenhagen, Denmark
[46] University Observatory Munich, Scheinerstrasse 1, 81679 München, Germany
[47] Max Planck Institute for Astronomy, Königstuhl 17, 69117-Heidelberg, Germany
[48] Institute of Theoretical Physics, Charles University, V Holešovičkách 2, 18000 Prague, Czech Republic
[49] Bellatrix Observatory, via Madonna de Loco 47, 03023 Ceccano, Italy
[50] Dipartimento di Fisica, Università di Salerno, Fisciano, INFN, sez. di Napoli, IIASS, Vietri sul Mare, Italy
[51] Armagh Observatory, College Hill, Armagh, BT61 9DG, UK
[52] Department of Physics, Sharif University of Technology, PO Box 11155-9161, Tehran, Iran
[53] Institut für Astrophysik, Georg-August Universität, Friedrich-Hund-Platz 1, 37077 Göttingen, Germany
[54] Institut d'Astrophysique et de Géophysique, Allée du 6 Août, Sart Tilman, Bât. B5c, 4000 Liège, Belgium
[55] Astrophysics Group, Keele University, Newcastle-under-Lyme, ST5 5BG, UK
[56] INAF, Osservatorio Astronomico di Brera, 23846 Merate (LC), Italy
[57] Deutsches SOFIA Institut, Universität Stuttgart, Pfaffenwaldring 31, 70569 Stuttgart, Germany
[58] SOFIA Science Center, NASA Ames Research Center, Mail Stop N211-3, Moffett Field CA 94035, USA
[59] Department of Astronomy, Kyoto University, 606-8502 Kyoto, Japan
[60] School of Mathematical Sciences, Queen Mary University of London, Mile End Road, London E1 4NS, UK
[61] The Wendelstein Calar Alto Pixellensing Project, http://www.usm.uni-muenchen.de/people/arri/wecapp.html
[62] Possum Observatory, Patutahi, Gisbourne, New Zealand
e-mail: john_drummond@xtra.co.nz
[63] School of Physics and Astronomy and Wise Observatory, Tel-Aviv University, Tel-Aviv 69978, Israel
e-mail: [shai;dani;shporer;david]@wise.tau.ac.il
[64] Auckland Observatory, Auckland, New Zealand
e-mail: gwchristie@christie.org.nz
[65] Farm Cove Observatory, Centre for Backyard Astrophysics, Pakuranga, Auckland, New Zealand
e-mail: farmcoveobs@xtra.co.nz
[66] Kiso Observatory, Institute of Astronomy, The University of Tokyo, 10762-30, Mitake, Kiso, 397-0101 Nagano, Japan
[67] Teide Observatory
[68] The Graduate University for Advanced Studies (Sokendai), 2-21-1 Oosawa, Mitaka, 181-8588 Tokyo, Japan
[69] CALMIP, DTSI Université Paul Sabatier, Université de Toulouse 31062 Toulouse, France
[70] Perimeter Institute for Theoretical Physics, 31 Caroline Street North, Waterloo, ON N2L 2Y5, Canada
[71] Korea Astronomy and Space Science Institute,776 Daedukdae-ro, Yuseong-gu, 305-348 Daejeon, Republic of Korea (South Korea)
[72] International Institute for Advanced Scientific Studies, via G. Pellegrino 19, 84019 – Vietri sul Mare (SA), Italy
[73] Department of Physics, University of Salerno, via Ponte Don Melillo, 84084 – Fisciano (SA), Italy
[74] Department of Physics & Astronomy, Aarhus Universitet, Ny Munkegade, 8000 Aarhus C, Denmark
[75] Molehill Astronomical Observatory, Auckland, New Zealand
[76] Departamento de Astronomía y Astrofísica, Universidad de Valencia, 46100 Burjassot, Valencia, Spain
[77] Dept. of Physics, Texas A&M University, College Station, TX, USA
[78] Institute for Advanced Study, Einstein Drive, Princeton, NJ 08540, USA
[79] AUT University, Auckland, New Zealand
[80] Okayama Astrophysical Observatory, National Astronomical Observatory of Japan, Asaguchi, 719-0232 Okayama, Japan

Pages 11 to 12 are available in the electronic edition of the journal at http://www.aanda.org

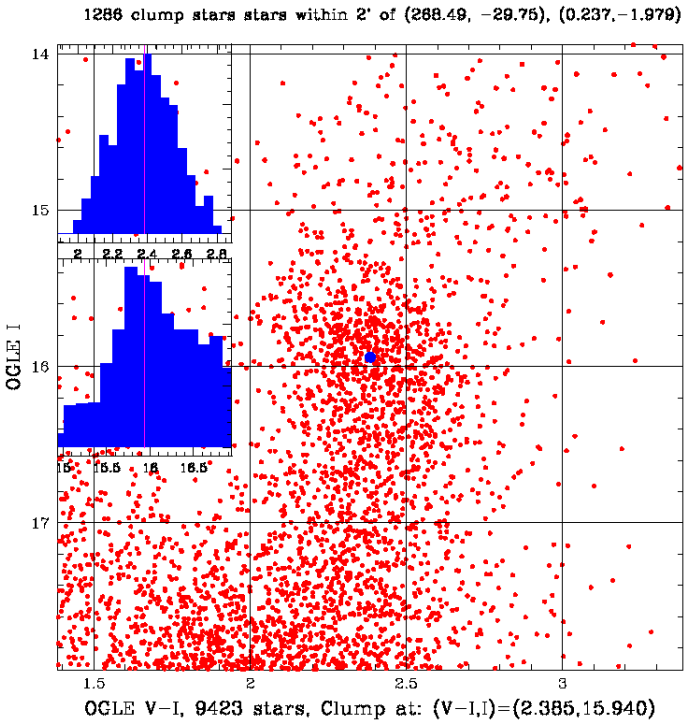

Fig. A.1. Colour–magnitude diagram in I and V from calibrated OGLE-III photometry. The superimposed histograms show the position of the centroid of the RGC.

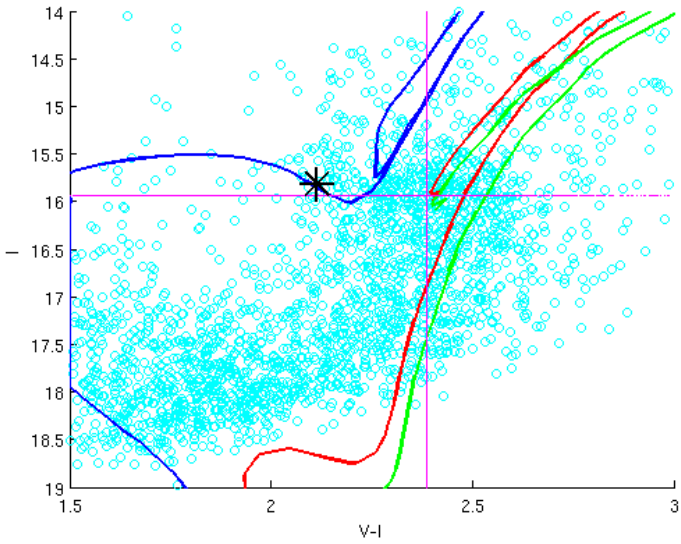

Fig. A.2. The V and I colour–magnitude diagram similar to Fig. 3, but now with superimposed isochrones from Marigo et al. (2008) for solar metallicity and three different ages: 0.6 Gyr (blue), 5 Gyr (red) and 10 Gyr (green), assuming a distance modulus of 14.6, an extinction $E(V-I) = 1.30$ and $R_I = 1.11$. The black star symbol marks the position of the source.

Appendix A: V, $(V-I)$ CMD

A colour–magnitude diagram allows an estimate of the dereddened magnitude and colour of the target, by comparison with the observed position of the RGC, if one assumes that both suffer the same amount of extinction. We retrieved stars within 2′ of the target in the OGLE-III photometric catalogue of field BLG 101.3, and constructed the calibrated CMD shown in Fig. A.1 (Szymański et al. 2011). From it, we measured the RGC centroid position, which is $I^{\rm RC} = 15.940 \pm 0.010$ and $(V-I)^{\rm RC} = 2.385 \pm 0.005$, and relative shifts in magnitude and colour of the three stars close to the target position, for which we found the values given in the last two columns of Table 2.

Unlike in previous studies, we do not fix the absolute magnitude of the RGC at some standard value, because the population corrections to apply to the well determined local clump position are somewhat uncertain. For instance, Salaris & Girardi (2002) give corrections for Baade's Window in V varying from 0.06 to 0.21 depending whether one adopts scaled-solar or α-enhanced metallicities. If one also changes the underlying adopted SFR (star formation rate) and AMR (age-metallicity relation), the corrections further vary, as shown in Girardi & Salaris (2001). We prefer using the same isochrone method as in the near-infrared to fit the RGC and giant branch positions. We adopt for this purpose the Marigo et al. (2008) set of isochrones, as given on their web site[2].

Our parameters are now the extinction $E(V-I)$ and the total-to-selective absorption ratio R_I. An acceptable fit is shown in Fig. A.2. It uses $E(V-I) = 1.30$ and $R_I = 1.11$. The first value is in good agreement with a similar determination at the target position in the OGLE-II BUL_SC3 field as reported by Sumi (2004), namely $E(V-I) = 1.336$. The agreement is not expected to be perfect, first because the OGLE-III transmission curves in I and V differ slightly from those of OGLE-II, and second because Sumi assumes an RGC intrinsic colour of 1.028, slightly different from the value we obtain. The second value is larger than the mean value adopted by Sumi (2004), which is 0.964, but in good agreement with an independent determination based on the recently released OGLE-III photometric catalogue of the Galactic bulge, which gives an average value of $R_I = 1.22$ (Nataf et al. 2012). All these values are clearly lower than the standard value of this ratio, which is 1.5, justifying the so-called anomalous extinction law generally invoked when dealing with the Galactic bulge (see, e.g. Udalski 2003).

From the adopted values of these two parameters, we derive absorption values for the field of $A_I = 1.44$ and $A_V = 2.74$. For the measured position of the RGC and our adopted distance modulus, the mean absolute magnitudes of the RGC are found to be $M_I = -0.10$ and $M_V = 0.98$. The standard values for the RGC colour and magnitude adopted in Nataf et al. (2012) are $(V-I)_\circ = 1.06 \pm 0.12$ and $M_I = -0.12 \pm 0.09$, in good agreement with our derivation.

Assuming once more that the source suffers the same amount of extinction as the RGC, and using the shifts in magnitude and colour listed in Table 2, the source is predicted to have $I_\circ^{\rm S} = 14.37$ and $(V-I)_\circ{}^{\rm S} = 0.82$. Using the previously derived values of the near-infared magnitudes of the source, we get a colour $(V-K)_\circ = 1.9$. All these colours point to an early G giant spectral type.

From the adopted dereddened magnitudes and colours, and using the revision of the surface brightness-colour relations in $I_\circ$, $(V-I)_\circ$ published by Kervella & Fouqué (2008), we get an estimate of the angular source radius θ_* in μas of

$$\log\theta_* = -0.2I_\circ + 0.4895(V-I)_\circ - 0.0657(V-I)_\circ^2 + 3.198. \quad \text{(A.1)}$$

The uncertainty of this estimate is 0.0238, so adding quadratically the uncertainty in magnitude (0.1) and colour (0.05) to this

[2] http://stev.oapd.inaf.it/cgi-bin/cmd_2.2

gives an accuracy of 9% on θ_*, i.e., $\theta_* = 4.8 \pm 0.4\,\mu$as. This confirms the previous result derived from the $V_\circ$, $(V-K)_\circ$ surface brightness-colour relation.

Note that, for this colour determination, we assumed that the star, OGLE-III-BLG-101.3 159762 in Table 2, is the source star. But in the MOA frames, the three stars in Table 2 are not fully resolved. The two OGLE stars close to the source, 160107 and 160108, can therefore contribute a blend flux in our models. In microlensing modelling we have to take this blend flux into account. Had we obtained calibrated data, we could have predicted the blend and source fluxes using our models. Unfortunately, the reduction we used for our modelling is not calibrated. We therefore used the original reduction of MOA data, which is calibrated but of lower quality, to estimate the blend properties. We found that the colour and magnitude of this blend corresponds to the sum of the fluxes of the 160107 and the 160108 stars. This means that our identification of the three OGLE stars was correct. In any case, future adaptive optics observations would be useful to confirm our conclusions.